Article:
Kessar, M, Hughes, DW orcid.org/0000-0002-8004-8631, Kersale, E et al. (2 more authors) (2019) Scale Selection in the Stratified Convection of the Solar Photosphere. Astrophysical Journal, 874 (1). 103. ISSN 0004-637X

https://doi.org/10.3847/1538-4357/ab07bf

Draft version January 24, 2019
Typeset using LaTeX **twocolumn** style in AASTeX61

SCALE SELECTION IN THE STRATIFIED CONVECTION OF THE SOLAR PHOTOSPHERE

Mouloud Kessar[1]

David W. Hughes[1]

Evy Kersalé[1]

Krzysztof A. Mizerski[2]

Steven M. Tobias[1]

[1] *Department of Applied Mathematics*
University of Leeds
Leeds LS2 9JT
UK
[2] *Department of Magnetism*
Institute of Geophysics
Polish Academy of Sciences
ul. Ksiecia Janusza 64
01-452 Warsaw
Poland

(Received February, 2018; Revised; Accepted)

Submitted to ApJ

ABSTRACT

We examine the role of stratification in determining the length scales of turbulent anelastic convection. Motivated by the range of scales observed in convection at the solar photosphere, we perform local numerical simulations of convection for a range of density contrasts in large domains, analyzing both the Eulerian and Lagrangian statistics of the flow. We consider the two cases of constant dynamic viscosity and constant kinematic viscosity. We discuss the implications of our results to the issue of solar mesogranulation.

Keywords: Sun, Photosphere — convection — stratification — granules – mesogranules

Corresponding author: Mouloud Kessar
m.kessar@leeds.ac.uk

1. INTRODUCTION

Convection in the solar photosphere is characterized by a wide range of scales. The smallest clearly discernible scale is that of the granules; granular convection itself has a range of scales, with a typical granule being 1Mm in horizontal extent and having a lifetime of a few minutes. The kinetic energy contained in these scales is transferred to smaller scales through a turbulent cascade, until it is dissipated as heat at scales of the order of a millimetre. At a considerably larger scale are the supergranules, with a typical size of 30Mm and a lifetime of a few days. The existence of granular and supergranular scales is clear from numerous observational studies (e.g. Rieutord & Rincon 2010; Hathaway et al. 2015). There is, however, an additional putative intermediate convective scale, known as *mesogranulation*. A mesogranular scale of convection was first reported by November et al. (1981), who used time-averaged velocity measurements to identify a convective scale of the order of 4Mm with a lifetime of about two hours. Intriguingly though, there is no specific signature detectable in the kinetic energy spectra at this scale that would unambiguously identify a true mesogranular scale, distinct from either large granules or small supergranules (see Hathaway et al. 2000; Rieutord & Rincon 2010, and references therein). The existence of mesogranulation has thus been the subject of considerable debate over the last few decades.

From a theoretical perspective, several computational studies have addressed the modelling of mesogranulation. The first such studies, which employed the Boussinesq approximation (Cattaneo et al. 2001, 2003), did indeed observe larger-scale convective structures, which could be identified as mesogranules, together with smaller cells, which could be identified as granules. In order to go beyond the Boussinesq approximation by incorporating the influence of stratification — a crucial ingredient of the solar photosphere — the problem of convective cell structure has also been addressed using codes that solve the fully compressible convection equations. For instance, Rincon et al. (2005), Bushby et al. (2012) and Bushby & Favier (2014) investigated fully compressible convection, though for quite small density contrasts. They also observed the emergence of large convective cells, of a similar scale to those seen in the Boussinesq configuration; in these studies, mesogranules were associated with the most energetic scale in the kinetic energy spectrum. From the point of view of terminology, when comparing the results of simulations with solar observations, certain studies (e.g. Rieutord & Rincon 2010; Hathaway et al. 2015) associate the highly energetic convective cells with granules, whilst others (e.g. Bushby et al. 2012; Bushby & Favier 2014) refer to these as mesogranules.

Although the effects of density stratification are of course included in the equations of fully compressible convection, the numerical constraints involved in accurately tracking sound waves are severe, ensuring that only fairly small density contrasts can be studied. However, in the Sun, the density stratification close to the surface is pronounced, with a change in density of nearly four orders of magnitude over the outer 2% of the Sun (Stix 1989). Here, therefore, we propose to study the pivotal role of density stratification by considering the problem of thermal convection under the anelastic approximation, an asymptotic reduction of the full governing equations that retains the effects of stratification, but filters out sound waves (see Gough 1969; Lantz & Fan 1999). Such an approach has been employed for a number of years in global spherical simulations of stars and planets (e.g. Glatzmaier & Gilman 1981; Clune et al. 1999). However, for local models with Cartesian geometries, the development of this types of codes is, somewhat surprisingly, rather new. A review of the various computational approaches that have been employed to model stellar convection is provided by Kupka & Muthsam (2017).

The outline of the paper is as follows. Section 2 presents the mathematical formulation of the problem of thermal convection in the anelastic approximation, with a brief description of the numerical approach we have employed (a fuller description can be found in the Appendix). Section 3 describes the results of the numerical simulations for the case of constant dynamic viscosity, employing three different approaches to investigating the dependence of the convective cell structure on the stratification of the atmosphere. Section 4 examines the changes that arise in the case when the kinematic viscosity is assumed constant. The connection with the long-standing issue of solar mesogranulation is discussed in Section 5.

2. MATHEMATICAL FORMULATION OF ANELASTIC CONVECTION

We consider the problem of anelastic convection between two infinite horizontal planes, at $z = 0$ (bottom) and $z = d$ (top). This orientation of the z-axis, opposite to that traditionally used for compressible convection, allows for a formal identification of the anelastic and Boussinesq equations. Several different formulations of the anelastic approximation can be found in the literature. Here we follow that introduced by Lantz & Fan (1999); the results of this formulation have been compared with those of fully compressible convection, both

in the linear (Berkoff et al. 2010) and nonlinear regimes (Verhoeven et al. 2015).

The starting point for the anelastic approximation is to decompose the density ρ, temperature T, pressure p and entropy s into an adiabatic, z-dependent reference state, indicated by overbars, and a perturbation to this state, indicated by subscripts "1":

$$\rho = \rho_r\left(\bar{\rho}+\varepsilon\rho_1\right), \qquad T = T_r\left(\overline{T}+\varepsilon T_1\right),$$
$$p = p_r\left(\bar{p}+\varepsilon p_1\right), \qquad s = s_r + c_p\varepsilon\left(\bar{s}+s_1\right), \tag{1}$$

where c_p is the specific heat at constant pressure, and ρ_r, T_r, p_r and s_r are representative values of the density, temperature, pressure and entropy, evaluated at the bottom of the layer. The asymptotically small parameter ε is a dimensionless measure of departure from adiabaticity, expressed as

$$\varepsilon = -\frac{d}{T_r}\left(\frac{\mathrm{d}\overline{T}}{\mathrm{d}z}+\frac{g}{c_p}\right), \tag{2}$$

where $\boldsymbol{g} = -g\,\boldsymbol{e}_z$ is the gravity vector.

The reference state depends only on the height z, and takes the form of a polytrope:

$$\bar{\rho} = (1+\theta z/d)^m, \quad \overline{T} = 1+\theta z/d, \quad \bar{s} = \frac{1}{|\theta|}\ln(1+\theta z/d), \tag{3}$$

where $\theta < 0$ is the dimensionless temperature difference across the layer and $m = 3/2$ is the adiabatic polytropic index. The density contrast across the layer is defined by

$$\chi = \frac{\bar{\rho}(0)}{\bar{\rho}(d)} = \frac{1}{(1+\theta)^m}. \tag{4}$$

In this formulation of the anelastic approximation, it is assumed that the effect of the molecular transport of heat and momentum is much smaller than that induced by turbulent motions. Hence we introduce a turbulent thermal diffusivity κ, and a turbulent kinematic viscosity ν, with representative values at $z = 0$ of κ_r and ν_r respectively, together with an entropy based diffusion (see Braginsky & Roberts 1995). Furthermore, we assume that the thermal conductivity, $k = \bar{\rho}\,c_p\,\kappa$, is constant (and hence κ varies with depth).

On scaling lengths with the layer depth d, and times with the thermal relaxation time d^2/κ_r, the evolution of the perturbations to the reference state in the velocity $\boldsymbol{u}$, and entropy s, (dropping subscripts "1") is governed by the following dimensionless set of equations (e.g. Mizerski & Tobias 2011):

$$\frac{\partial \boldsymbol{u}}{\partial t} + \boldsymbol{u}\cdot\nabla\boldsymbol{u} = -\nabla\left(\frac{p}{\bar{\rho}}\right) + RaPr\,s\,\boldsymbol{e}_z + Pr\,\boldsymbol{D}_v, \tag{5}$$

$$\nabla.\left(\bar{\rho}\boldsymbol{u}\right) = 0, \tag{6}$$

$$\frac{\partial s}{\partial t} + \boldsymbol{u}\cdot\nabla s = \frac{u_z}{1+\theta z} + \frac{1}{\bar{\rho}}\left(\nabla^2 s + \frac{\theta}{\overline{T}}\frac{\partial s}{\partial z}\right) + C_q\,Q, \tag{7}$$

with

$$Q = 2\sum_{i=1}^{3}\left(\frac{\partial u_i}{\partial x_i}\right)^2 + \frac{2}{3}\left(\nabla\cdot\boldsymbol{u}\right)^2 + \sum_{i<j}^{3}\left(\frac{\partial u_i}{\partial x_j}+\frac{\partial u_j}{\partial x_i}\right)^2. \tag{8}$$

The quantities $\boldsymbol{D}_v$ and C_q take different forms dependent on the choice of prescription for the viscosity. If the dynamic viscosity, $\mu = \bar{\rho}\,\nu$, is assumed constant, then

$$\boldsymbol{D}_v = \frac{1}{\bar{\rho}}\left(\nabla^2\boldsymbol{u} + \frac{1}{3}\nabla\left(\nabla\cdot\boldsymbol{u}\right)\right), \qquad C_q = \frac{-\theta}{Ra\overline{T}\bar{\rho}}. \tag{9}$$

Conversely, if the kinematic viscosity is assumed constant, then

$$\boldsymbol{D}_v = \nabla^2\boldsymbol{u} + \frac{1}{3}\nabla\left(\nabla\cdot\boldsymbol{u}\right) + \frac{\mathrm{d}\ln\bar{\rho}}{\mathrm{d}z}\left(\frac{\partial\boldsymbol{u}}{\partial z} + \nabla u_z - \frac{2}{3}(\nabla\cdot\boldsymbol{u})\boldsymbol{e}_z\right),$$
$$C_q = \frac{-\theta}{Ra\overline{T}}. \tag{10}$$

The Rayleigh number Ra and Prandtl number Pr appearing in equation (5) are constants, defined by their values at the bottom of the layer:

$$Ra = \frac{gd^3\varepsilon}{\nu_r\kappa_r}, \qquad Pr = \frac{\nu_r}{\kappa_r}. \tag{11}$$

For stratified convection, one may also define z-dependent versions of the Rayleigh and Prandtl numbers, $Ra(z)$ and $Pr(z)$, defined as in (11) but with ν and κ rather than ν_r and κ_r. For constant μ, $Ra(z) \propto \bar{\rho}^2$, $Pr(z) =$ constant; for constant ν, $Ra(z) \propto \bar{\rho}$, $Pr(z) \propto \bar{\rho}$.

An important aspect of the above formulation of the anelastic equations is that the Boussinesq equations are recovered exactly by imposing $\theta = 0$; in this case the variable s is identified not with the entropy, but with the temperature.

We consider a domain that is square and periodic in the horizontal directions, of size $\lambda\times\lambda\times 1$. On $z = 0$ and $z = 1$, we adopt stress-free and impermeable velocity boundary conditions; the system is also assumed to have uniform entropy (with $s = 0$) on $z = 0$ and $z = 1$. The layer of fluid is initially at rest with only small random entropy perturbations.

We have developed a computational code to solve the anelastic equations (5)–(7) in a Cartesian domain.

Derivatives in the horizontal directions are computed using FFTs, via the FFTW library, and in the vertical direction by a 4th order finite-difference representation. Time stepping is achieved through a semi-implicit scheme, in which the nonlinear terms are treated by a second order Adams-Bashforth method and the linear terms by a Crank-Nicolson scheme. The pressure is handled via a poloidal-toroidal decomposition. Implementation of the boundary conditions requires use of the influence matrix method (Boronski & Tuckerman 2007). The code has been parallelized using MPI, with a pencil-based decomposition. Further details of the numerical approach are contained in the Appendix.

3. STRATIFIED ANELASTIC CONVECTION: CONSTANT DYNAMIC VISCOSITY

In this section, we concentrate on the case of constant dynamic viscosity μ, and explore the influence of density stratification on thermal convection by considering four representative cases. As our benchmark example, we consider Boussinesq (unstratified) convection (i.e. $\theta = 0$), for which a direct comparison can be made with the results of Cattaneo (1999). We then consider three further anelastic configurations (AC) with non-zero (negative) values of θ: a mildly stratified case with $\theta = -0.6$, giving a density contrast χ across the layer of $\chi = 4$ (AC4); a strongly stratified case with $\theta = -0.92$ and $\chi = 50$ (AC50); and an intermediate case with $\theta = -0.89$ and $\chi = 30$ (AC30). Following Cattaneo (1999), for the BC simulation we set $Ra = 500\,000$, $Pr = 1$ and $\lambda = 10$; if Ra_c denotes the critical Rayleigh number for the onset of convection, then the degree of supercriticality is given here by $Ra/Ra_c \approx 760$. As the stratification is increased, it becomes harder to drive convection, i.e. Ra_c increases (see e.g. Currie & Tobias 2016). Thus, to make meaningful comparisons between the three cases, we increase Ra for the AC runs in order to maintain the same degree of supercriticality at reference level $z = 0$; the parameter values are summarized in Table 2.

We consider the formation and evolution of the convective network from three different perspectives. In Section 3.1 we describe the broad features of the convection for the four cases by considering the distribution of the temperature (for the Boussinesq case) or the entropy (for the anelastic cases); in Section 3.2 we look in detail at how the network evolves in time by calculating the dispersion of a passive scalar introduced into the flow; in Section 3.3 we analyse the time-averaged convective network by considering the spectral distribution of kinetic energy. Rather than discuss the convection in terms of granules or mesogranules, in these sections we shall refer to either convective cells or the convective network.

3.1. *Convective Networks*

Figure 1 shows the temporal evolution of the volume-averaged kinetic energy E for the four cases. After an initial (linear) phase of exponential growth, the energy settles into a statistically stationary state. It is interesting to note that, although the degree of supercriticality (i.e. Ra/Ra_c) is the same for all four cases, there is some variation in the level of the energy in the saturated state and, furthermore, that the dependence of E on θ is non-monotonic.

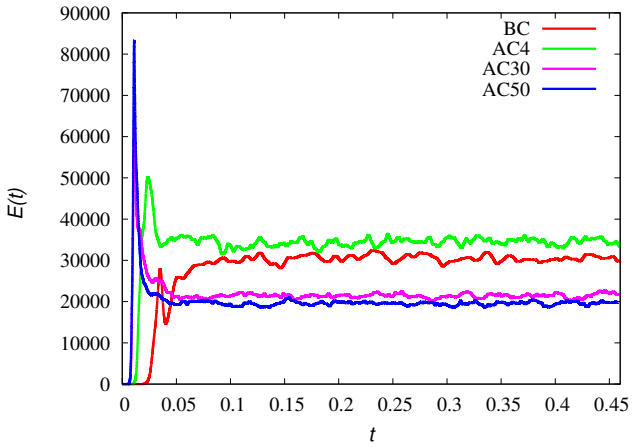

Figure 1. Time evolution of the averaged kinetic energy $E(t)$ for the four configurations.

The influence of stratification can be seen clearly in Figure 2, which depicts horizontal slices of temperature or entropy fluctuations at different depths for cases BC

Table 2. Parameter values for the four cases: λ is the aspect ratio, Pr is the Prandtl number, θ and χ are, respectively, the temperature difference and corresponding density contrast across the layer, Ra is the Rayleigh number and Ra_c its critical value for convection.

Parameters	BC	AC4	AC30	AC50
λ	10	10	10	10
Pr	1	1	1	1
θ	0	-0.60	-0.89	-0.92
χ	1	4	30	50
Ra	5×10^5	1.2×10^6	2.65×10^6	2.95×10^6
Ra_c	657.51	1566.89	3503.18	3885.07

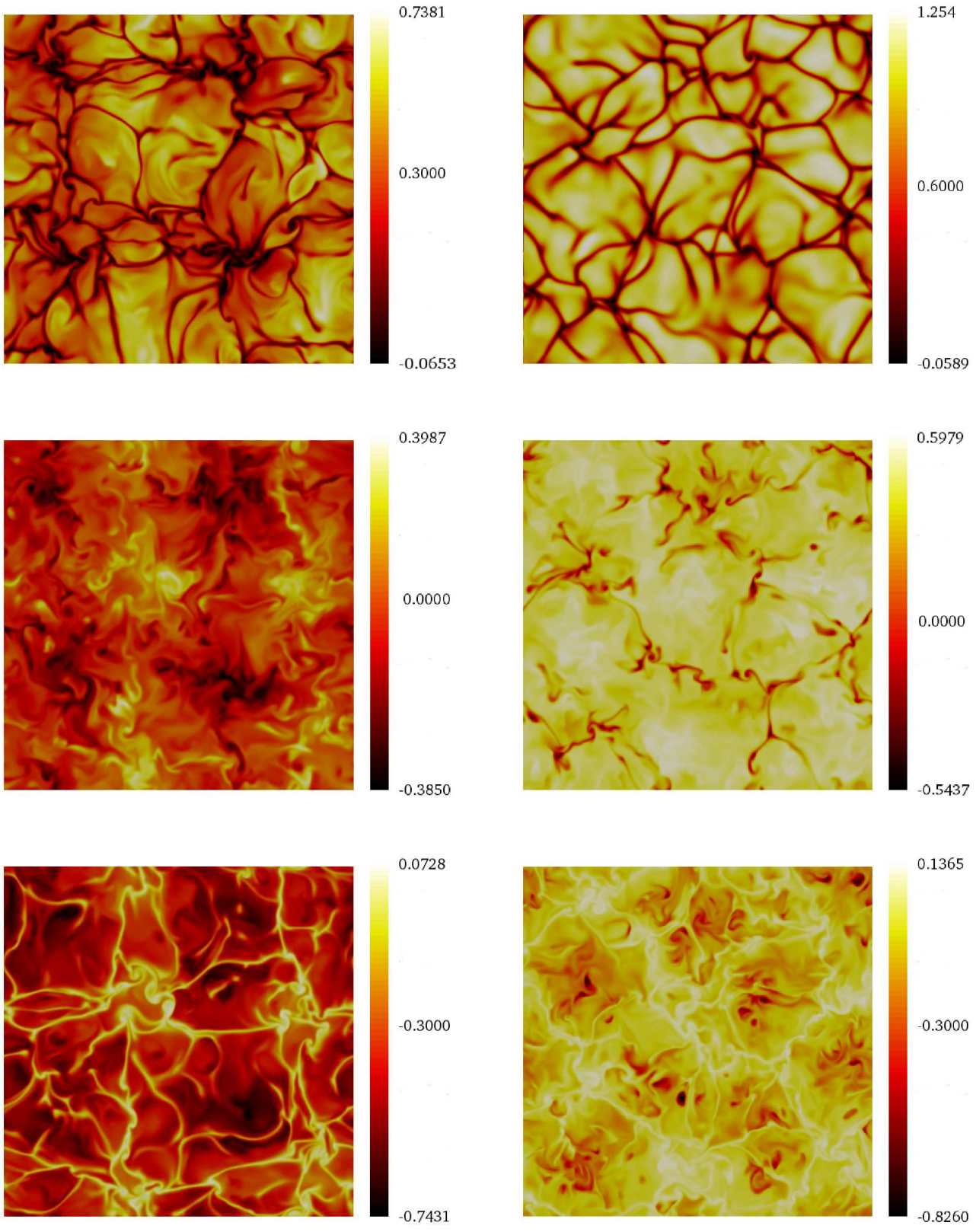

Figure 2. Horizontal slices of (a) temperature fluctuations for BC, and (b) entropy fluctuations for AC4, at heights $z = 0.9$ (top), $z = 0.5$ (middle) and $z = 0.1$ (bottom).

and AC4. Boussinesq convection is characterized by a symmetry about the mid-plane ($z = 0.5$), as can be seen from the general morphology of the convective networks towards the bottom and top of the domain. Near the bottom ($z = 0.1$), one can see a network of convective cells of different sizes, together with turbulent motions; the large convective cells are associated with warm upflows. Near the top of the domain ($z = 0.9$), the network of cells is similar to that at the bottom, but now with convective cells delineated by cold downflows. As expected from the Boussinesq symmetry, the BC case does not exhibit any particularly distinct cells or structures on the mid-plane. For anelastic convection, the z-symmetry is broken, as can be seen clearly for the case of AC4 shown in Figure 2b. At the top of the domain, there is a convective network with a range of scales, not dissimilar to that of Boussinesq convection. On the mid-plane, the outline of some of the largest cells are still discernible; as previously observed by Bushby et al. (2012), only the strongest downflows penetrate deeply into the convective region. At the bottom of the domain, and in sharp contrast to the Boussinesq case, there is no vestige of the convective network; the flow is highly turbulent, interspersed with light bridges depicting warm upflows.

In order to explore any influence of the horizontal extent of the domain, we have also performed the BC and AC4 simulations at the larger aspect ratio of $\lambda = 20$. Figure 3 shows horizontal slices at $z = 0.9$ of temperature (BC) and entropy (AC4) for these two additional configurations, which should be compared with the corresponding cases for $\lambda = 10$, shown in the top row of Figure 2. The general structure and characteristic sizes of the cells are very similar for the $\lambda = 10$ and $\lambda = 20$ cases, suggesting that with $\lambda = 10$ the convection is not strongly constrained by the size of the domain. It should though be pointed out that in the BC case at the larger aspect ratio, the largest convective cells can have more degrees of freedom for their orientation.

The nature of the convective network for the strongly-stratified AC50 case can be seen in Figure 4, which shows slices of the entropy fluctuations and the vertical vorticity at three heights in the domain. There is now a marked asymmetry between the top and bottom of the domain. Considering the entropy near the top of the domain, there is a well-defined laminar network of cells, with no evidence of turbulent small-scale behavior. Comparison with the network for the BC configurations (Figure 2a) shows that the largest convective cells observable are somewhat smaller in the strongly-stratified case. Associated with the network in the entropy fluctuations is a corresponding emerging network of vertical

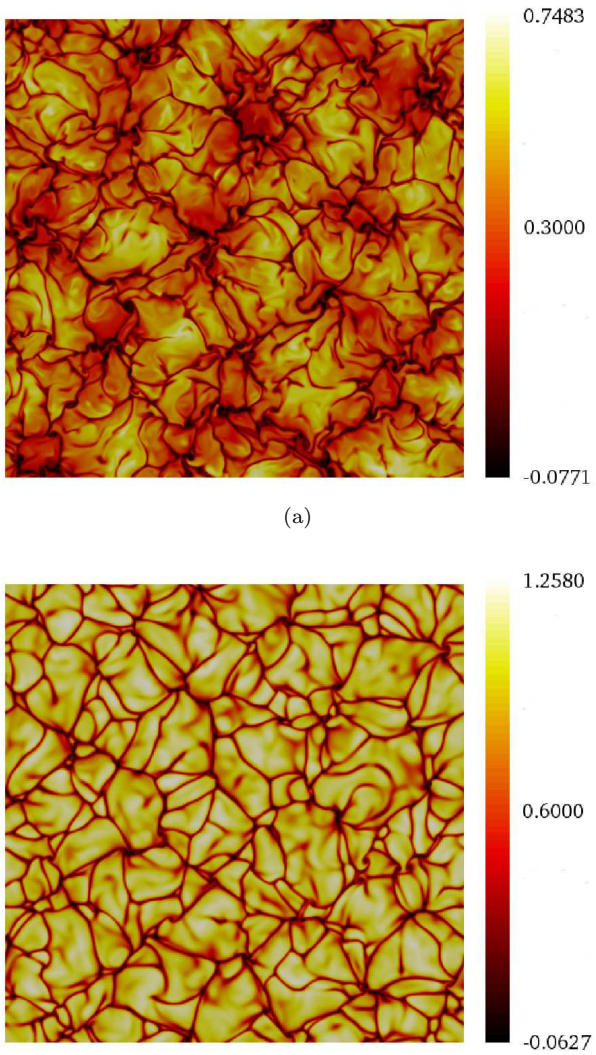

Figure 3. Horizontal slices of (a) temperature fluctuations for BC, and (b) entropy fluctuations for AC4, both with aspect ratio $\lambda = 20$; the height $z = 0.9$.

vorticity; small patches of concentrated vorticity form where the convective cells merge. As for the mildly-stratified (AC4) case, it is only the cells of greatest horizontal extent that propagate deeply; at the mid-plane, the imprint of the largest cells at the surface survives, visible in both the entropy and vorticity. At the bottom of the domain the flow is turbulent, which is particularly evident in the distribution of vertical vorticity, with no evidence remaining of the convective network.

Corresponding convective patterns can also be identified in the velocity components. Figure 5 shows horizontal slices of all three components of the velocity for the AC50 case, taken at the same time as the entropy snapshots in Figure 4. As has been widely observed in

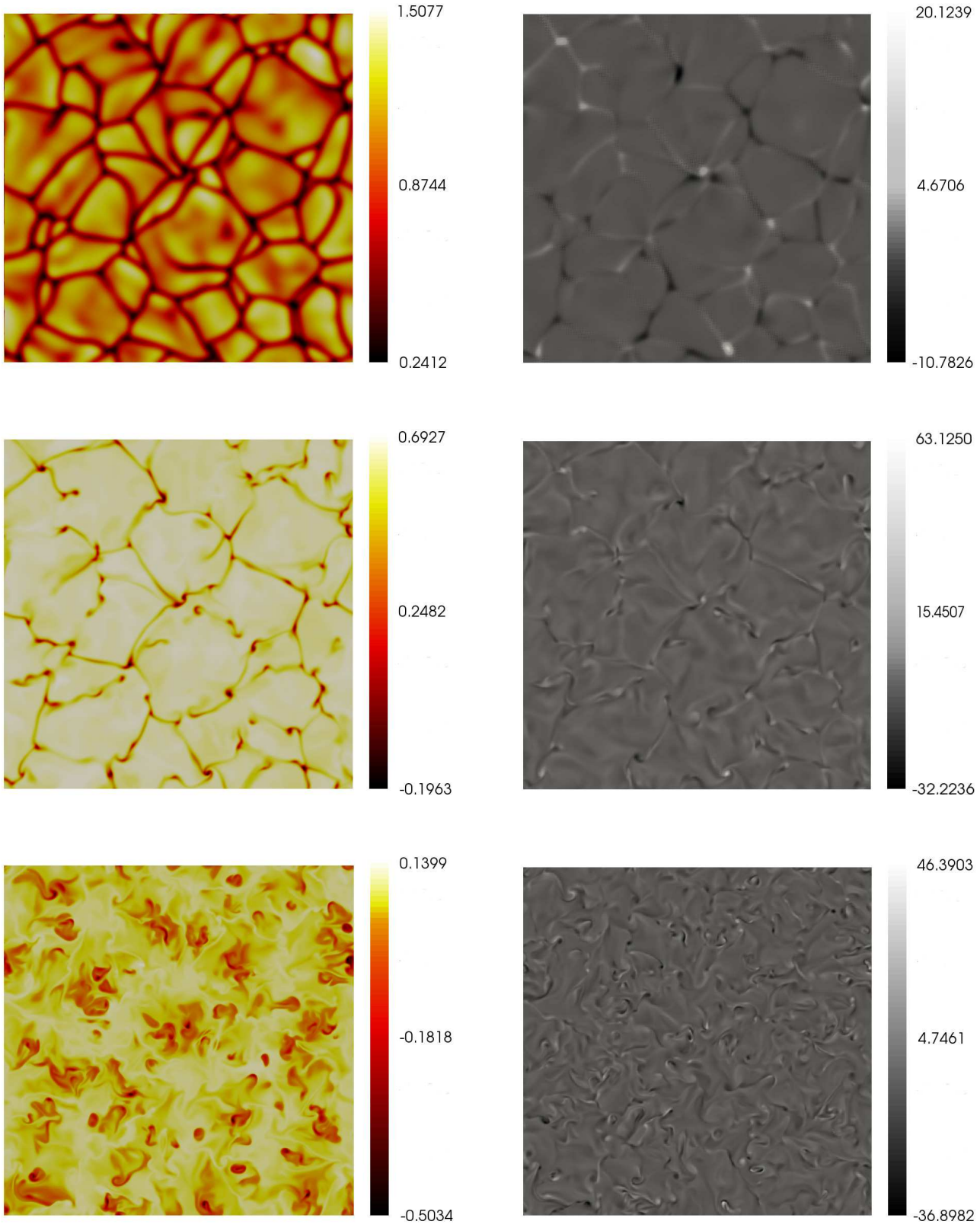

Figure 4. Horizontal slices of (a) entropy fluctuations and (b) vertical vorticity for the AC50 configuration, at heights $z = 0.9$ (top row), $z = 0.5$ (middle), and $z = 0.1$ (bottom).

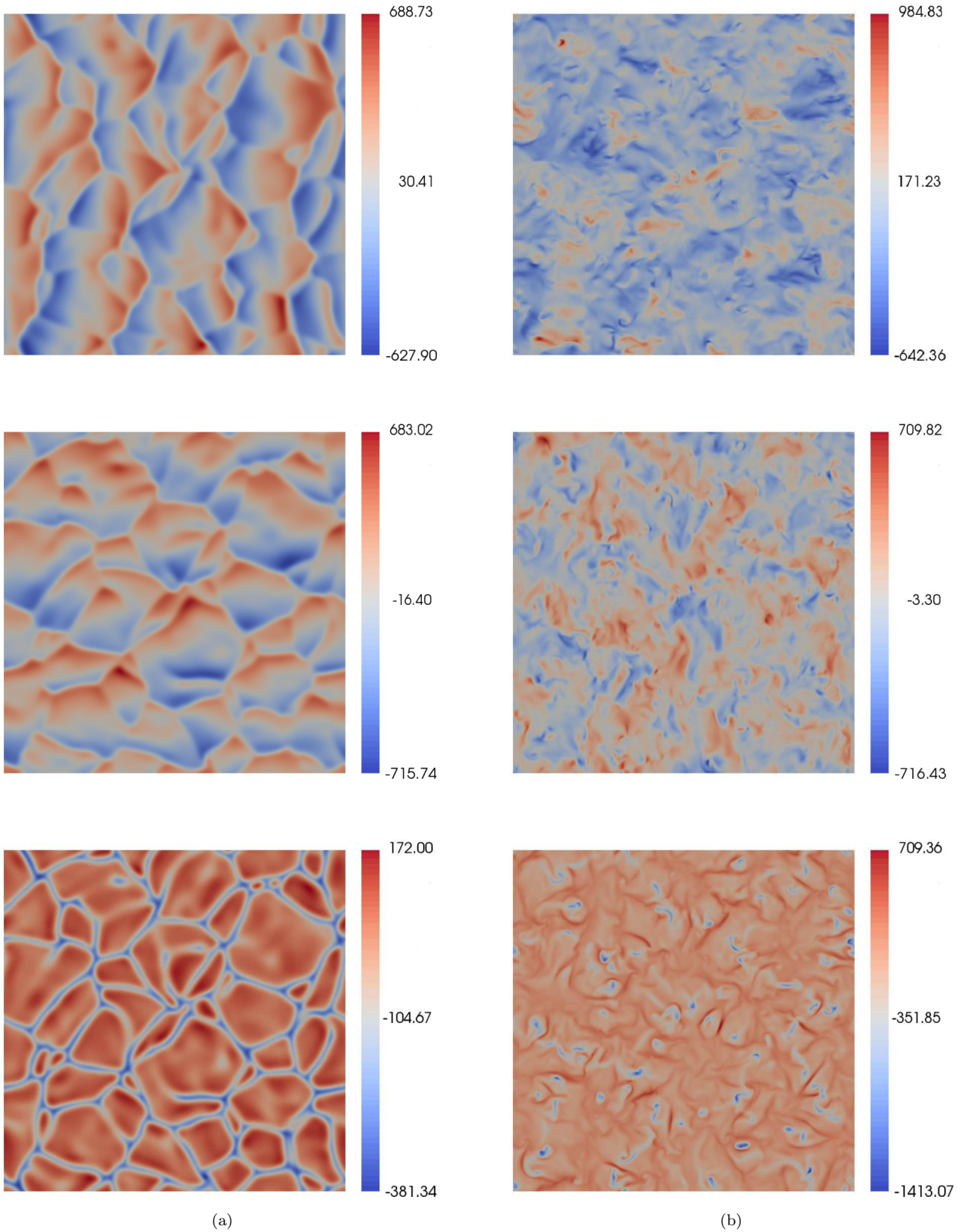

Figure 5. Horizontal slices at (a) $z = 0.9$ and (b) and $z = 0.1$ for the AC50 configuration, for the velocity components in the x (top row), y (middle), and z (bottom) directions, taken at the same time as the snapshots in Figure 4.

previous simulations of convection, at the top of the domain there is a strong correlation between the vertical velocity and the entropy fluctuations; thus all scales of the convective network are evident. In the horizontal velocity components, by contrast, only the large-scale convective cells can be identified. Near the bottom of the domain, where the flow is highly turbulent, the convective network is less evident — as it is in the entropy distribution. The vertical velocity and entropy fluctuations are again correlated, and some structures can be identified; this is no longer the case for the horizontal components.

3.2. *Influence of the Convective Network on a Passive Scalar*

A complementary approach to visualising the convective network (which samples its Eulerian representation), and particularly to tracking its temporal evolution, is to compute the motion of passive tracer particles or 'corks' (therefore, to some extent, gaining insight into the horizontal Lagrangian statistics). This idea was first introduced by Simon & Weiss (1989) in order to understand the evolving photospheric network. Simon & Weiss (1989) considered a model cellular flow and showed how the corks, advected solely by the horizontal component of the velocity, first moved to map out a linear network, before congregating in isolated concentrations at longer times; such behavior is reminiscent of the radial magnetic field observed in the photosphere. The notion of tracking corks has subsequently been used in numerical simulations of convectively-driven flows (Cattaneo et al. 2001; Bushby & Favier 2014), in which the corks are again advected into the interstices of the convective network.

An alternative, though related, approach to tracking the motion of discrete passive tracer particles is to consider the temporal evolution of a continuous passive scalar — what we shall refer to here as 'ink'. In particular, we consider the advection by the horizontal velocity of an initially uniform distribution of ink. If the scalar field ϕ denotes the concentration of ink, then its evolution is governed by the advection-diffusion equation

$$\frac{\partial \phi}{\partial t} + \nabla_h \cdot (\boldsymbol{u}\phi) = S_c(z)\nabla_h^2 \phi, \tag{12}$$

where the subscript h denotes horizontal derivatives. For numerical expediency, we take the Schmidt number S_c to be a function of z. We are interested in the pattern mapped out by the ink on various horizontal planes; given the changes in the flow characteristics with depth, it turns out to be convenient to have S_c increasing as $1/\bar{\rho}$, with the value of unity at $z = 0$.

Here we consider the evolution of the passive scalar for the strongly stratified case (AC50). The ink is introduced at some time t_0 in the fully nonlinear stationary regime. Figure 6 shows snapshots of the distribution of ink near the top and bottom of the domain at three representative times. At the top of the domain, the ink is pushed quickly between the cells, mapping out the convective network, as shown by the distribution at $t' = t - t_0 = 0.00375$. The ink then starts to become concentrated at the corners of the cells, but with the overall network still visible, as shown by the plot at $t' = 0.009075$. The long-term distribution, as shown by the plot at $t' = 0.0525$, is marked by a disjoint concentration of ink at the corners of the convective network. The behavior at the bottom of the domain is slightly different. At $t' = 0.00375$, there is a hint of a network emerging, but, owing to the turbulent motions, it is much harder to distinguish than near the top. At $t' = 0.009075$, a clearer network is emerging at the bottom of the domain, although the turbulent motions are still visible. At long times ($t' = 0.0525$), the ink again accumulates in a few locations, although, in contrast to the top of the domain, it is redistributed by the turbulent motions. The most noticeable characteristics of the evolution of a continuous passive scalar — its accumulation between convective cells and its redistribution by the turbulent motions — are very similar to those observed by Bushby et al. (2012) in a weakly stratified system using discrete tracer particles.

3.3. *Spectral Distribution of Kinetic Energy*

In Sections 3.1 and 3.2 we have seen the emergence of a convective network through the temporal evolution of the entropy and of a passive scalar. Here we supplement these studies by investigating the spectral distribution of kinetic energy. In order to do so, we employ a formulation of the kinetic energy spectrum used extensively in simulations of turbulent convection (e.g. Bushby et al. 2012). For a given height z, and time t, we evaluate the spectral distribution of kinetic energy

$$E_k(k_h, z, t) = \frac{\bar{\rho}(z)}{2} \sum_{k_x} \sum_{k_y} |\hat{\boldsymbol{u}}_{k_x,k_y}(z,t)|^2, \tag{13}$$

where $\hat{\boldsymbol{u}}_{k_x,k_y}$ is the two-dimensional Fourier transform (in horizontal planes) of the velocity field, with the summations over all horizontal wavenumbers such that $k_x^2 + k_y^2 = k_h^2$. We also consider the separate decompositions of the energies of the horizontal and vertical motions.

Figure 7 shows spectra for the four cases, which have been both depth averaged and time averaged over 10–15 turnover times. In this figure alone, the energy spec-

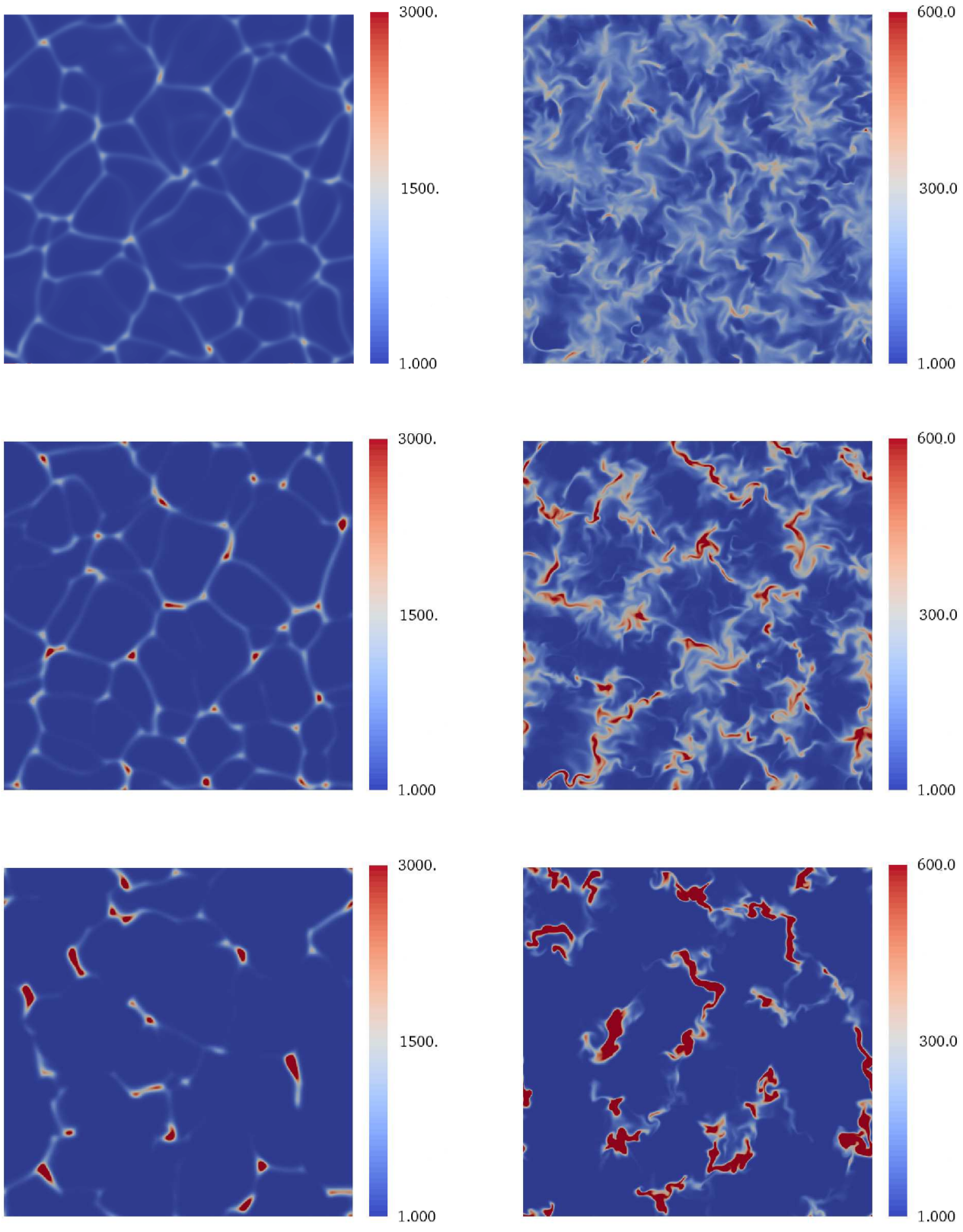

Figure 6. Distribution of ink at (a) $z = 0.9$ and (b) $z = 0.1$ at elapsed times $t' = 0.00375$ (top), $t' = 0.009075$ (middle) and $t' = 0.0525$ (bottom) for the AC50 configuration. Initially (i.e. $t' = 0$) the ink is uniformly distributed with a value arbitrarily fixed to $\phi = 100$. The color scale is the same for all plots, chosen to cover the entire range at $t' = 0.00375$. The turnover time is $\tau \approx 0.025$ at $z = 0.9$, and $\tau \approx 0.036$ at $z = 0.1$. The top row corresponds to the same time as the snapshots in Figures 4 and 5.

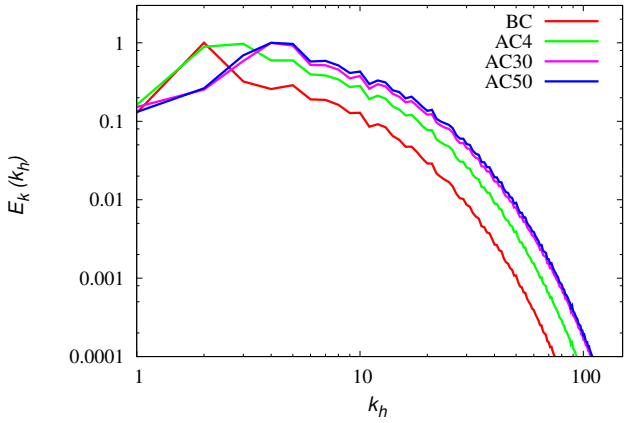

Figure 7. Time- and depth-averaged kinetic energy spectra for the four different cases.

tra have been normalized so that the changes in spatial scales between the different cases become more apparent. There is a clear peak of energy at a large scale, with the peak moving to a larger wavenumber (smaller scale) as the stratification increases. The difference between the BC and AC4 cases remains small, but is more significant in the cases of AC30 and AC50, which are very similar.

Whereas Figure 7 provides an idea of the distribution of energy over horizontal scales for the domain as a whole, it is important also to consider the energy distribution at different heights. Figure 8 shows the kinetic energy spectra at $z = 0.1$, 0.5 and 0.9 for the AC4 and AC50 cases. Two significant observations can be made. First, the effect of the midplane symmetry of the layer can still be observed at large scales for the weakly stratified case but not for the case of strong stratification. In the latter, the kinetic energy is in fact significantly reduced with height, particularly at small scales; this is consistent with the snapshots of the entropy and the passive scalar presented earlier and also with the studies of compressible convection by Bushby et al. (2012) and Bushby & Favier (2014). From equations (5) and (7), it can be seen that the dissipation terms scale as $1/\bar{\rho}$ (through $\boldsymbol{D}_v$ and C_q); the dissipation therefore increases with height, suppressing any small-scale turbulence near the top of the domain. The second point to note is that, even for the strongly stratified case, the most energetic scale does not change with depth, as noted by Bushby et al. (2012) in their mildly stratified, fully compressible simulations. The results for the BC configuration are not shown here, but the spectra at $z = 0.1$ and $z = 0.9$ are identical, owing to the Boussinesq symmetry.

Figure 9 shows, separately, time- and depth-averaged spectra of the kinetic energy associated with horizontal and vertical motions, for the BC, AC4 and AC50 cases (AC30 and AC50 being extremely similar). At large scales, the bulk of the energy is contained in the horizontal motions. We note also that the migration to smaller scales with increasing stratification can be seen equally in both the horizontal and vertical spectra.

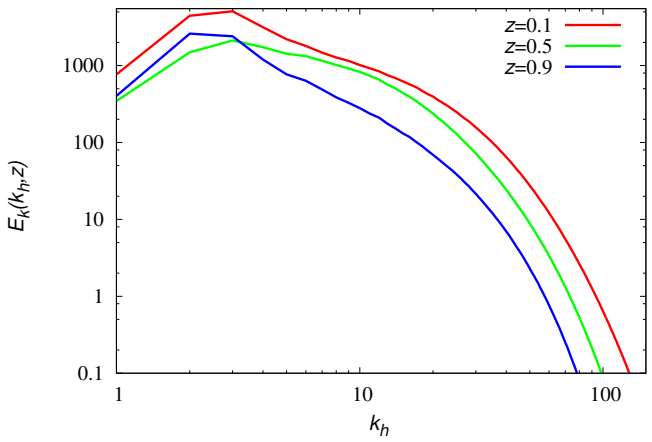

(a)

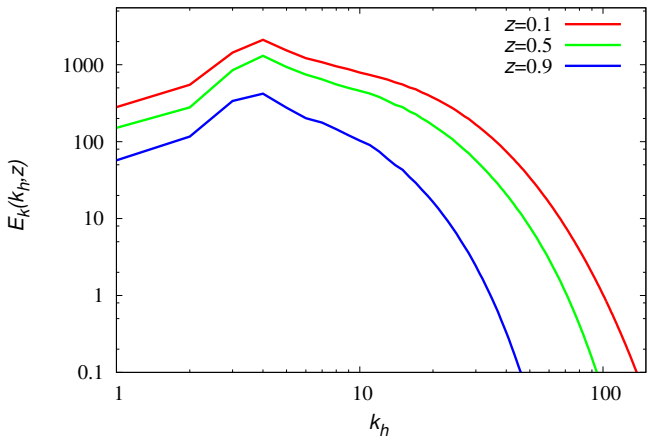

(b)

Figure 8. Kinetic energy spectra at different heights for (a) AC4 and (b) AC50 configurations.

In addition, Figure 10 shows time-averaged spectra of the kinetic energy contained in the horizontal and vertical motions for the AC50 case at three different depths. At each depth, the horizontal motions are dominated by the large scales; there is a well-defined peak in the spectrum, but also significant energy in the largest scales possible. By contrast, the vertical motions have little energy in the very largest scales, but there is then a plateau in the spectrum over a range of wavenumbers, before the energy falls off at large k. At the top of the layer, these

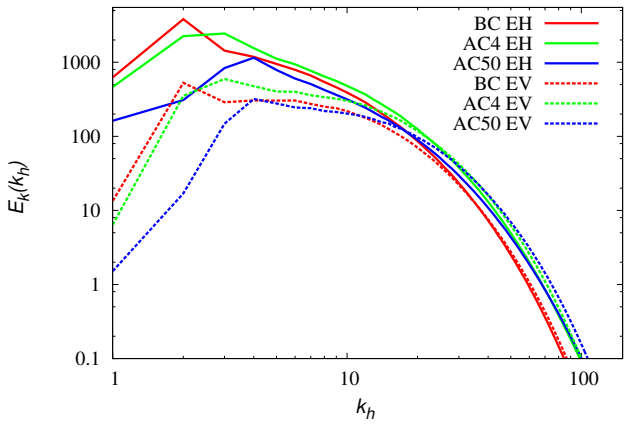

Figure 9. Time- and depth-averaged spectra of the energy contained in the horizontal motions (EH) and in the vertical motions (EV).

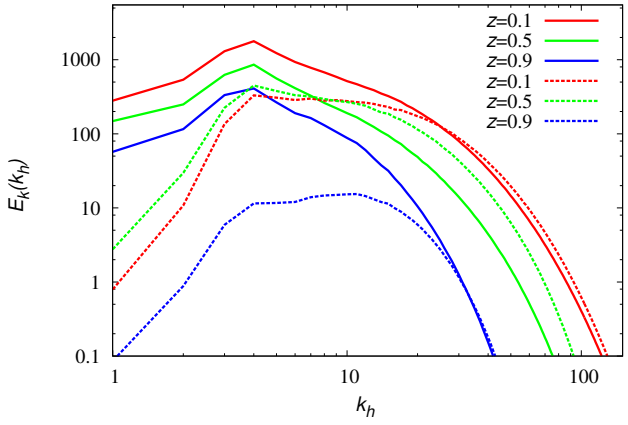

Figure 10. Time-averaged spectra of the energy contained in the horizontal motions (solid lines) and in the vertical motions (dashed lines), at different heights for AC50.

spectra are consistent with the plots in Figure 5a, in which there is an absence of small granules in the snapshots of the horizontal velocity components, but a wider range of scales in the vertical velocity. At depth, where the motions are much more turbulent, such features are less apparent (Figure 5b), even though the shapes of the spectra are essentially the same at all depths.

Finally, Figure 11 presents instantaneous spectral distributions of the fluctuations of ink and entropy at depths $z = 0.1$ and $z = 0.9$, obtained at the same time-step as the snapshots in Figure 6. The most significant feature is that the spectra of the two different quantities are extremely similar: at both depths, they have a peak at the same wavenumber, which corresponds to that of the peak in the kinetic energy spectrum. Thus,

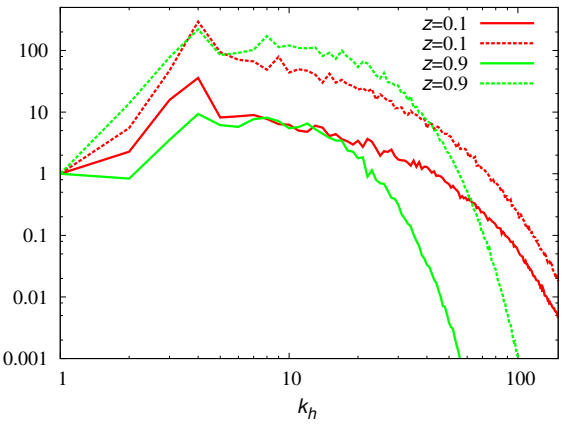

Figure 11. Spectral distributions of entropy (solid lines) and ink (dashed lines) at $t' = 0.00375$ for $z = 0.9$ (green) and $z = 0.1$ (red) in the AC50 case. Data were normalized to the intensity of the spectral distribution at the lowest wave number.

as expected, the dominant scale in both the entropy fluctuations and the ink is that of the horizontal motions.

4. CONSTANT KINEMATIC VISCOSITY

As described in the introduction, two possible, widely used prescriptions for the viscosity are those of constant dynamic viscosity and constant kinematic viscosity. The results of the previous section were obtained for the case of constant μ; it is therefore of interest also to consider the case of constant ν, and to examine whether the main conclusions still hold. To this end, in this section we study the AC30 configuration (see Table 2), but with constant ν, and compare the results against those obtained for AC30 with constant μ. Recall, from Section 2, that $Ra(z)$ decreases with height more slowly for the case of constant ν. Unsurprisingly therefore, with all other parameters the same, the degree of supercriticality is higher for the case of constant ν; the average kinetic energy $\langle E_k \rangle \approx 2.2 \times 10^4$ for constant μ, whereas $\langle E_k \rangle \approx 2.8 \times 10^4$ for constant ν.

4.1. *Convective Networks*

In order to investigate the influence of the particular prescription for the viscosity, we first consider the nature of the convective networks. Figure 12 compares snapshots of the entropy slices at three depths for the two cases of constant dynamic viscosity and constant kinematic viscosity. For both configurations the flow is highly turbulent at the bottom of the domain, and a convective network is hard to identify. Conversely, near

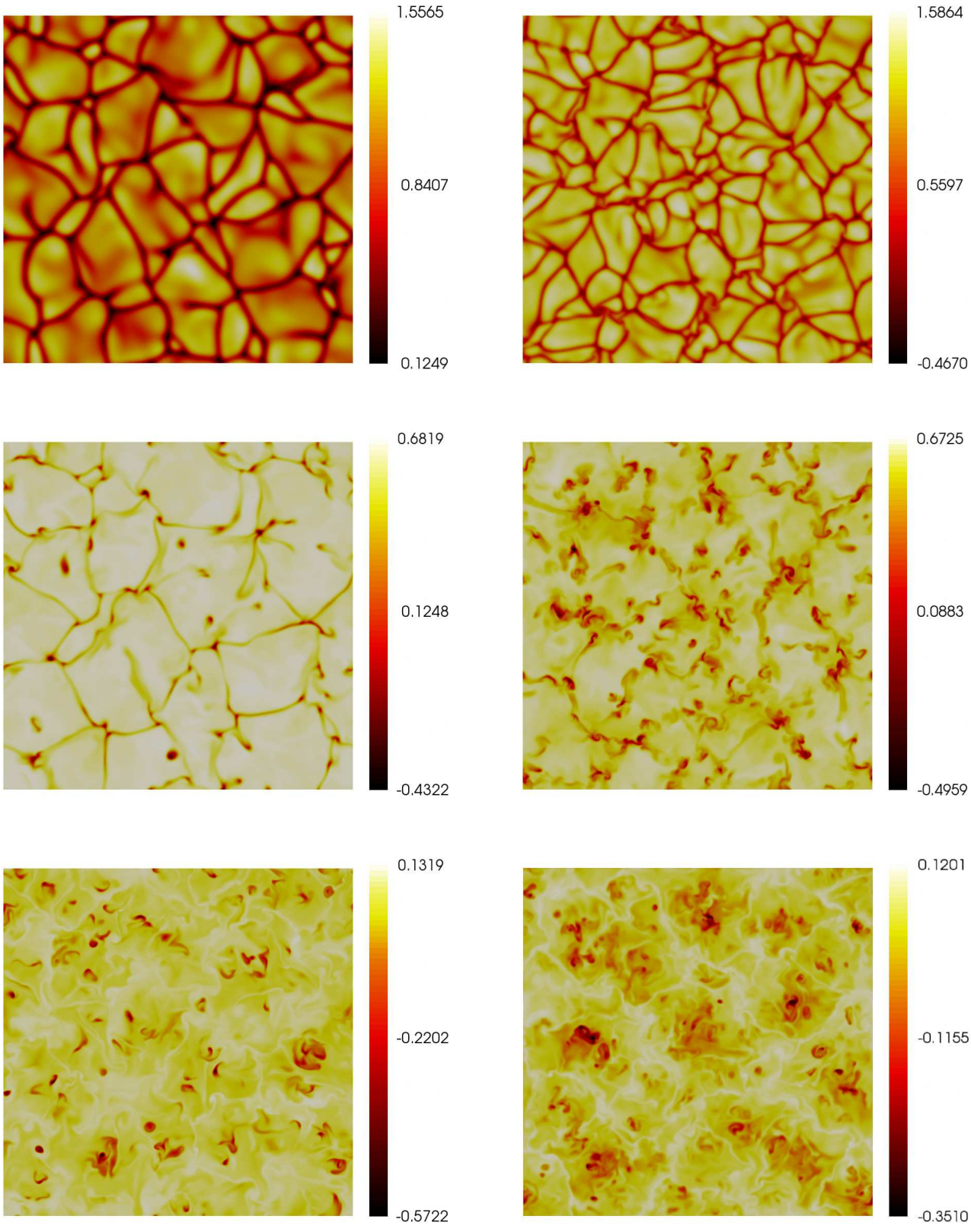

Figure 12. Horizontal slices of entropy fluctuations for the AC30 configuration, at heights $z = 0.9$ (top row), $z = 0.5$ (middle), and $z = 0.1$ (bottom), with (a) constant dynamic viscosity and (b) constant kinematic viscosity.

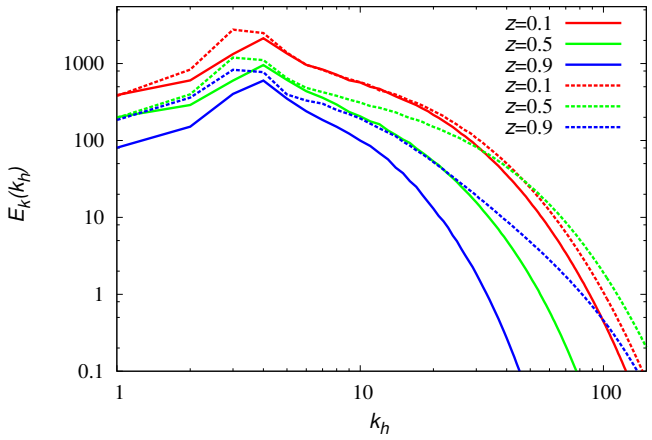

(a)

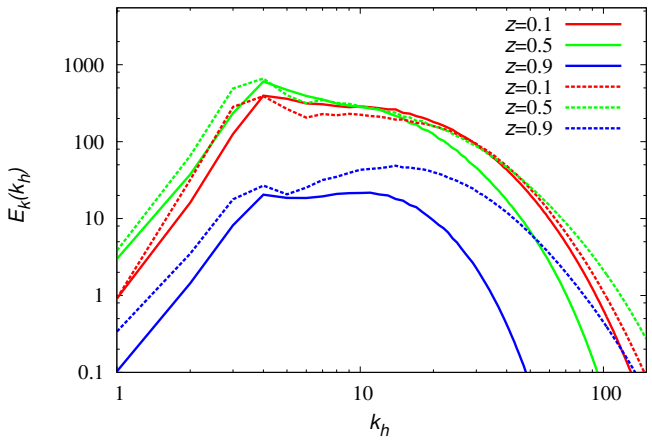

(b)

Figure 13. Time-averaged spectra of the kinetic energy contained (a) in the horizontal motions and (b) in the vertical motions, at different heights, for AC30 with constant dynamic viscosity (solid lines) and constant kinematic viscosity (dashed lines).

the top, a clear network is apparent in both cases, with a range of convective cell sizes. The main difference between the two cases is that the turbulence extends further into the domain for constant kinematic viscosity. This is evidenced by comparison of the entropy snapshots at $z = 0.5$; whereas the network is clearly outlined in the case of constant dynamic viscosity, the cell boundaries, though discernible, are much more turbulent for the case of constant kinematic viscosity.

4.2. *Spectral Distribution of Kinetic Energy*

As in Section 3, it is instructive to complement the visualisation of the convective network obtained through snapshots of the flow with an analysis of the spectra of the horizontal and vertical kinetic energies. Figure 13 shows the spectral distribution of the kinetic energy contained in the horizontal and vertical motions at different depths, for both prescriptions of the viscosity. As expected from the entropy snapshots in Figure 12, there is increased energy in the small scales for the case with constant kinematic viscosity, in both the vertical and horizontal motions. On the other hand, the energies in the large scale structures are close. The kinetic energy is dominated by the horizontal motions; for these, the most energetic convective scale is the same at all depths and for both configurations. Interestingly, near the top of the layer, the dominant scale of the weaker vertical motions is smaller than that established by the dominant horizontal flows. Thus, the choice of viscosity prescription influences the small scales and the degree of turbulence, but has little impact on the highly energetic convective cells observed at large scales.

5. DISCUSSION

In this paper we have investigated the role of stratification in modifying spatial scale selection in a local model of anelastic convection. By employing the computationally more tractable anelastic approximation, we have been able to study density ratios far in excess of those attainable in fully compressible models. Both the Eulerian and Lagrangian properties of the turbulent convection are modified by the presence of strong stratification. The midplane symmetry of the Boussinesq approximation is broken as the stratification is increased, leading to convection that has a well-defined, reasonably laminar cellular structure near the top of the domain, but a much more turbulent nature at depth. Furthermore, the initial increase in stratification away from the unstratified case produces a marked shift to smaller-scale convection, as can be seen from comparison of the energy spectra for the BC and AC4 cases. However, it is of interest to note that, for a given degree of supercriticality, the convective structure eventually becomes independent of further increases in the stratification, the spectra of AC30 and AC50 being essentially identical. Our main focus has been on the case for which the dynamic viscosity μ and the thermal conductivity k are constant, and hence the kinematic viscosity ν and thermal diffusivity κ increase with height. We have though, for comparison, also considered one case in which the kinematic viscosity is constant. Although the overall nature of the convection — i.e. laminar cell structure near the surface but with more turbulent flows at depth — is unchanged, the suppression of small-scale turbulence with height is less pronounced.

From our simulations it is clear that in the upper regions of the domain there is a characteristic scale of convection, as shown in Figures 2 and 4. From study of the dispersion of a passive scalar, it can be seen that the dominant scale is essentially the largest scale that emerges from the smaller-scale convective cells. One might therefore deem this to be the 'mesogranular' scale. What is important to note though is that this scale cannot be attributed to a different physical formation mechanism to the smaller-scale 'granular' convection. The presence or absence of this dominant mesogranular large-scale has been attributed to the dynamics of vorticity, with strong vortex patches on small scales leading to the formation of such dominant scales (Bushby & Favier 2014). Our simulations for strong stratifications lend support to this theory. Furthermore, it is of interest to note that changing from a constant dynamic viscosity μ to a constant kinematic viscosity ν does not affect the small-scale vorticity sufficiently to suppress the formation of the dominant scale. It is though worth pointing out that it is very difficult to pick out spatial scales from spectral analysis since the lack of phase information leads to sharp gradients in the velocity across a wide range of scales. A wavelet and multifractal analysis of the type performed by Lawrence et al. (1997) for solar magnetic fields may prove more revealing. Finally, we note that by identifying the 'granular scale' as the most energetic scale, as is also typically done observationally, the granular scale does not change with depth. If, alternatively, one were to define a 'typical' granule size, then this would increase with depth (for example, from comparison of the entropy slices at $z = 0.9$ and $z = 0.5$ in Figure 4).

We conclude by discussing possibilities for further investigations. At large enough scales, rotational effects will cease to be negligible; it will therefore be important to consider extended domains in order to identify how far down the spectrum the effects of rotation are felt. This will have direct relevance for understanding the interactions in the Sun between all scales from supergranules to granules. Furthermore, it is also of interest to identify how reducing the thermal Prandtl number to more realistic values affects scale selection and energy transport. Our study to date has been purely hydrodynamic. Work is in progress to extend this to consider the interaction between the convection and magnetic fields; more precisely, we shall investigate both the processing of large-scale flux generated elsewhere (thus modelling the injection of flux from a large-scale solar dynamo) and magnetic field generated by the small-scale dynamo action of the convection itself. The computationally tractable anelastic system considered here will allow the investigation of dynamo action in highly stratified turbulent domains.

This work was supported by STFC under grant ST/N000765/1. The computations were performed on ARC1 and ARC2, part of the High Performance Computing facilities at the University of Leeds, and on the COSMA Data Centric system at Durham University, operated by the Institute for Computational Cosmology on behalf of the STFC DiRAC HPC Facility (www.dirac.ac.uk). This equipment was funded by a BIS National E-infrastructure capital grant ST/K00042X/1, DiRAC Operations grant ST/K003267/1 and Durham University. DiRAC is part of the National E-Infrastructure. We are grateful to Laura Currie for her help in validating the computational code, and to the referee for useful comments that have improved the manuscript.

APPENDIX

A. NUMERICAL ALGORITHM

Here we give details of the numerical algorithm employed to solve the equations of anelastic convection (i.e. equations (5)–(7)) in Cartesian geometry. Since periodicity is assumed in the horizontal (x, y) plane, we adopt standard Fast Fourier Transforms in these directions; two dimensional Fourier coefficients are indicated with hats. The equations are discretized in z using a fourth order finite-difference scheme with an evenly spaced grid. They thus form large systems of algebraic equations, which we solve via an LU decomposition using the LAPACK library.

In the anelastic formalism, $\nabla \cdot (\bar{\rho}\mathbf{u}) = 0$ (equation (6)); hence $\langle u_z \rangle_h = 0$ and the momentum can be expressed as

$$\bar{\rho}\boldsymbol{u} = \bar{\rho}\langle u_x \rangle_h \boldsymbol{e}_x + \bar{\rho}\langle u_y \rangle_h \boldsymbol{e}_y + \nabla \times (\bar{\rho}\Gamma \boldsymbol{e}_z) + \nabla \times \nabla \times (\bar{\rho}\tilde{P}\boldsymbol{e}_z), \tag{A1}$$

where Γ and $\tilde{P}$ are toroidal and poloidal scalar fields respectively, and $\langle \cdot \rangle_h$ denotes a horizontal average. For simplicity in the notation we also introduce $P = \bar{\rho}\tilde{P}$.

The momentum equation (5) can then be expressed in terms of these toroidal and poloidal components. The evolution equation for P arises from the z component of the curl of the curl of the momentum equation whilst the evolution of

Γ is obtained from the z component of the curl of the momentum equation. The resulting equations are different for the two prescriptions of viscosity, so we consider these separately.

First we consider the case of constant dynamic viscosity μ. Then, in Fourier space for wavenumbers $(k_x, k_y) \neq (0,0)$, the evolution of $\hat{P}$ and $\hat{\Gamma}$ is governed by the following equations:

$$\frac{\partial \hat{\mathrm{D}}_-^2 \hat{P}}{\partial t} = \hat{N}_P + P_r \hat{\mathrm{D}}_-^2 \hat{\mathrm{D}}_-^2 \hat{P}, \tag{A2}$$

with

$$\hat{N}_P = -\frac{i}{k^2}\left(k_x \frac{\partial \hat{X}}{\partial z} + k_y \frac{\partial \hat{Y}}{\partial z}\right) - \hat{Z} - R_a P_r \hat{s} + \frac{4}{3}\frac{P_r m^2 \theta^2}{\bar{\rho}^2 (1+\theta z)^2} k^2 \hat{P}; \tag{A3}$$

and

$$\frac{\partial \hat{\Gamma}}{\partial t} = \hat{N}_\Gamma + \frac{P_r}{\bar{\rho}} \hat{\nabla}^2 \hat{\Gamma}, \qquad \text{with} \qquad \hat{N}_\Gamma = \frac{i}{k^2}\left(k_x \hat{Y} - k_y \hat{X}\right); \tag{A4}$$

here $k^2 = k_x^2 + k_y^2$, $X = -\boldsymbol{u} \cdot \nabla u_x$, $Y = -\boldsymbol{u} \cdot \nabla u_y$, $Z = -\boldsymbol{u} \cdot \nabla u_z$. The differential operators are defined by

$$\hat{\nabla}^2 = -k^2 + \frac{\partial^2}{\partial z^2}, \qquad \hat{\mathrm{D}}_-^2 = \frac{1}{\bar{\rho}}\left(\hat{\nabla}^2 - \frac{\mathrm{d}\ln\bar{\rho}}{\mathrm{d}z}\frac{\partial}{\partial z}\right). \tag{A5}$$

In addition, we need to consider the evolution of the horizontally averaged velocity. Both non-zero components are governed by the same equation, namely

$$\frac{\partial \langle u \rangle_h}{\partial t} = -\langle \mathbf{u} \cdot \nabla u \rangle_h + \frac{P_r}{\bar{\rho}} \frac{\partial^2 \langle u \rangle_h}{\partial z^2}, \tag{A6}$$

with $u = u_x$ or $u = u_y$.

For the case of constant kinematic viscosity ν, we first express $\boldsymbol{D}_v$ from expression (10) in the alternative form

$$\boldsymbol{D}_v = \nabla^2 \boldsymbol{u} + \frac{\mathrm{d}\ln\bar{\rho}}{\mathrm{d}z}\left(\frac{\partial \boldsymbol{u}}{\partial z} + \frac{2}{3}\nabla u_z + \frac{(2m+1)\theta}{3(1+\theta z)} u_z \boldsymbol{e}_z\right). \tag{A7}$$

The evolution of $\hat{P}$ and $\hat{\Gamma}$ is then governed by the following equations:

$$\frac{\partial \hat{\mathrm{D}}_-^2 \hat{P}}{\partial t} = \hat{N}_P + P_r \hat{\mathrm{D}}_+^2 \hat{\mathrm{D}}_-^2 \hat{P}, \tag{A8}$$

with

$$\hat{N}_P = -\frac{i}{k^2}\left(k_x \frac{\partial \hat{X}}{\partial z} + k_y \frac{\partial \hat{Y}}{\partial z}\right) - \hat{Z} - R_a P_r \hat{s} + \frac{P_r m \theta^2}{\bar{\rho}(1+\theta z)^2}\left(-\frac{\partial^2}{\partial z^2} + \frac{m\theta}{(1+\theta z)}\frac{\partial}{\partial z} + \frac{(3+2m)\theta k^2}{3}\right)\hat{P}; \tag{A9}$$

and

$$\frac{\partial \hat{\Gamma}}{\partial t} = \hat{N}_\Gamma + P_r \hat{\mathrm{D}}_+^2 \hat{\Gamma}, \qquad \text{with} \qquad \hat{N}_\Gamma = \frac{i}{k^2}\left(k_x \hat{Y} - k_y \hat{X}\right). \tag{A10}$$

The differential operator $\hat{\mathrm{D}}_+^2$ is defined by

$$\hat{\mathrm{D}}_+^2 = \hat{\nabla}^2 + \frac{\mathrm{d}\ln\bar{\rho}}{\mathrm{d}z}\frac{\partial}{\partial z}; \tag{A11}$$

note that the operators $\hat{\mathrm{D}}_-^2$ and $\hat{\mathrm{D}}_+^2$ differ not only in the sign of the second term, but also in the factor of $1/\bar{\rho}$.

The evolution of the horizontally averaged velocity in this case is governed by

$$\frac{\partial \langle u \rangle_h}{\partial t} = -\langle \mathbf{u} \cdot \nabla u \rangle_h + P_r \frac{\partial^2 \langle u \rangle_h}{\partial z^2} + P_r \frac{\mathrm{d}\ln\bar{\rho}}{\mathrm{d}z}\frac{\partial \langle u \rangle_h}{\partial z}, \tag{A12}$$

with $u = u_x$ or $u = u_y$.

The evolution equations for $\hat{P}$, $\hat{\Gamma}$, $\langle u_x\rangle_h$ and $\langle u_y\rangle_h$ must be complemented by either stress-free and impermeable boundary conditions, expressed as

$$\frac{\partial\langle u_x\rangle_h}{\partial z} = \frac{\partial\langle u_y\rangle_h}{\partial z} = 0 \quad \text{and} \quad \hat{P} = \hat{\mathrm{D}}_-^2\,\hat{P} = \frac{\partial\hat{\Gamma}}{\partial z} = 0 \quad \text{at } z = 0, 1; \tag{A13}$$

or no-slip and impermeable boundary conditions, which take the form

$$\langle u_x\rangle_h = \langle u_y\rangle_h = 0 \quad \text{and} \quad \hat{P} = \frac{\partial\hat{P}}{\partial z} = \hat{\Gamma} = 0 \quad \text{at } z = 0, 1. \tag{A14}$$

Using the same formalism, the evolution of entropy is governed, in Fourier space, by

$$\frac{\partial\hat{s}}{\partial t} = \hat{N}_s + \frac{1}{\bar{\rho}}\left(\hat{\nabla}^2 + \frac{\theta}{\overline{T}}\frac{\partial}{\partial z}\right)\hat{s}, \qquad \text{with} \qquad \hat{N}_s = \hat{S} + \frac{k^2\,\hat{P}}{\bar{\rho}(1+\theta z)} + C_q\hat{Q}, \tag{A15}$$

where $S = -\boldsymbol{u}\cdot\nabla s$, Q is defined in equation (8) and C_q is given either by equation (9) (constant μ) or (10) (constant ν). The boundary conditions for the entropy are $\hat{s} = 0$ at $z = 0, 1$.

We note that the Fourier modes $\hat{\Gamma}(k_x, k_y)$ and $\hat{s}(k_x, k_y)$, and the averaged velocities $\langle u_x\rangle_h$ and $\langle u_y\rangle_h$ are all solutions to formally similar mathematical problems, which can be expressed, for a generic field $F(t, z)$, as an evolution equation of the form

$$\frac{\partial F}{\partial t} = N_F + \mathrm{L}\,F, \tag{A16}$$

where N_F comprises nonlinear terms and L is a second order differential operator in space. Boundary conditions on F are either Dirichlet or Neumann conditions, namely $F = 0$ or $\partial F/\partial z = 0$ at $z = 0, 1$.

Here we describe in detail the procedure for advancing the generic field F in time. The linear and nonlinear terms in (A16) are treated separately. The linear terms are advanced using a second order Crank-Nicolson scheme, and the nonlinear terms by an explicit second order Adams-Bashforth scheme (with the first time step an Euler step). The time discretization of equations (A16) thus yields

$$\left(1 - \frac{\Delta_t}{2}\mathrm{L}\right)F^{n+1} = \frac{\Delta_t}{2}\left(3N_F^n - N_F^{n-1}\right) + \left(1 + \frac{\Delta_t}{2}\mathrm{L}\right)F^n, \tag{A17}$$

where the superscript n represents $t = n\Delta_t$, with Δ_t being a fixed time step. The system of algebraic equations resulting from the spatial discretization of (A17) and of the boundary conditions is solved, at every time step, for F^{n+1}. The algorithm described here applies straightforwardly to $\hat{\Gamma}(k_x, k_y)$, $\hat{s}(k_x, k_y)$, $\langle u_x\rangle_h$ and $\langle u_y\rangle_h$.

The poloidal field $\hat{P}(k_x, k_y)$ requires special attention however, owing to the form of the linear terms in the evolution equation (A2) and that of the boundary conditions. The case of stress-free boundary conditions, $\hat{P} = \hat{\mathrm{D}}_-^2\,\hat{P} = 0$ at $z = 0, 1$, can be treated readily in a two-step procedure partly analogous to that used for the other fields. First, noticing that (A2) is an equation of the form (A16), for $F = \hat{\mathrm{D}}_-^2\,\hat{P}$, with boundary conditions $F = 0$ at $z = 0, 1$, we use the algorithm (A17) to compute F^{n+1}. Then we solve, for P^{n+1}, the discretized version of the elliptic equation

$$\hat{\mathrm{D}}_-^2\,\hat{P}^{n+1} = F^{n+1} \quad \text{with } \hat{P}^{n+1} = 0 \text{ at } z = 0, 1. \tag{A18}$$

The implementation of no-slip boundary conditions, $\hat{P} = \partial\hat{P}/\partial z = 0$ at $z = 0, 1$, is however, not so straightforward and requires the use of Green's functions and the computation of an influence matrix (Boronski & Tuckerman 2007). Indeed, in this case, it is not possible to solve (A16) for $F = \hat{\mathrm{D}}_-^2\,\hat{P}$ as we have no information about $\hat{\mathrm{D}}_-^2\,\hat{P}$ at the boundaries. Instead, we discretize equation (A2) in time, again using Crank-Nicolson and Adams-Bashforth algorithms, and reformulate the discretized equation. At every time step, we first solve

$$\hat{\mathrm{D}}_-^2\,\hat{\Lambda}_0^{n+1} = \frac{\Delta_t}{2}\left(3\hat{N}_P^n - \hat{N}_P^{n-1}\right) \quad \text{with } \hat{\Lambda}_0^{n+1} = 0 \text{ at } z = 0, 1; \tag{A19}$$

once Λ_0^{n+1} is known, we can compute $\hat{P}_0^{n+1}$ by solving

$$\left(1 - \frac{P_r\Delta_t}{2}\hat{\mathrm{D}}_\mp^2\right)\hat{P}_0^{n+1} = \hat{\Lambda}_0^{n+1} + \left(1 + \frac{P_r\Delta_t}{2}\hat{\mathrm{D}}_\mp^{\,2}\right)\hat{P}^n \quad \text{with } \hat{P}_0^{n+1} = 0 \text{ at } z = 0, 1, \tag{A20}$$

where the operator $\hat{\mathrm{D}}^2_{\mp}$ becomes $\hat{\mathrm{D}}^2_{-}$ for the case of constant μ and $\hat{\mathrm{D}}^2_{+}$ for constant ν. At this stage, the poloidal component $\hat{P}_0^{n+1}$, the discrete solution of the evolution equation (A2), satisfies only one of the two sets of boundary conditions, $P_0^{n+1} = 0$ at $z = 0, 1$. We need to invoke Green's functions and the computation of an influence matrix to implement the second boundary conditions on $\hat{P}$. To achieve this, we construct, at every time step, a poloidal field consisting of $\hat{P}_0^{n+1}$ and a linear combination of two Green's functions,

$$\hat{P}^{n+1} = \hat{P}_0^{n+1} + a\,\hat{G}^{(1)} + b\,\hat{G}^{(2)}. \tag{A21}$$

The Green's functions $\hat{G}^{(1)}$ and $\hat{G}^{(2)}$ are computed, in preprocessing, by solving, for G, the time-independent linear equations

$$\hat{\mathrm{D}}^2_{-}\hat{\Lambda} = 0 \quad \text{and} \quad \left(1 - \frac{P_r\Delta_t}{2}\hat{\mathrm{D}}^2_{+}\right)\hat{G} = \hat{\Lambda}. \tag{A22}$$

This system is solved twice: once, for $G^{(1)}$, with boundary conditions

$$\hat{\Lambda} = 1 \text{ at } z = 0\ , \quad \hat{\Lambda} = 0 \text{ at } z = 1 \quad \text{and} \quad G = 0 \text{ at } z = 0, 1; \tag{A23}$$

and a second time, for $\hat{G}^{(2)}$, with boundary conditions

$$\hat{\Lambda} = 0 \text{ at } z = 0\ , \quad \hat{\Lambda} = 1 \text{ at } z = 1 \quad \text{and} \quad G = 0 \text{ at } z = 0, 1. \tag{A24}$$

Clearly, the poloidal field defined by (A21) satisfies the condition $\hat{P}^{n+1} = 0$ at $z = 0, 1$ and is the solution to the discretized evolution equation for $\hat{P}$,

$$\left(1 - \frac{P_r\Delta_t}{2}\hat{\mathrm{D}}^2_{\mp}\right)\hat{\mathrm{D}}^2_{-}\hat{P}^{n+1} = \frac{\Delta_t}{2}\left(3\hat{N}_P^n - \hat{N}_P^{n-1}\right) + \left(1 + \frac{P_r\Delta_t}{2}\hat{\mathrm{D}}^2_{\mp}\right)\hat{\mathrm{D}}^2_{-}\hat{P}^n. \tag{A25}$$

The coefficients a and b in the expression (A21) can then be chosen such that the second set of boundary conditions can be satisfied. Thus, $\partial\hat{P}^{n+1}/\partial z = 0$ at $z = 0, 1$ if a and b are solutions to the influence system

$$\begin{bmatrix} \partial_z\hat{G}^{(1)}(z=0) & \partial_z\hat{G}^{(2)}(z=0) \\ \partial_z\hat{G}^{(1)}(z=1) & \partial_z\hat{G}^{(2)}(z=1) \end{bmatrix} \begin{bmatrix} a \\ b \end{bmatrix} = - \begin{bmatrix} \partial_z\hat{P}_0^{n+1}(z=0) \\ \partial_z\hat{P}_0^{n+1}(z=1) \end{bmatrix}. \tag{A26}$$

Flows with stress-free boundary conditions can be computed in a similar fashion. Replacing the operator $\partial/\partial z$ by $\hat{\mathrm{D}}^2_{-}$ in the influence matrix guarantees that the condition $\hat{\mathrm{D}}^2_{-}\hat{P}^{n+1} = 0$ at $z = 0, 1$ is satisfied. For convenience, our numerical code uses influence matrices for both no-slip and stress-free boundary conditions. The additional computational cost of using Green's functions for stress-free boundary conditions, although not strictly required, is minimal.

When the horizontally-averaged velocity and both the toroidal and poloidal fields have been advanced in time, the velocity can be updated using

$$\mathbf{u} = \begin{bmatrix} \langle u_x\rangle_h \\ \langle u_y\rangle_h \\ 0 \end{bmatrix} + \begin{bmatrix} \dfrac{\partial\Gamma}{\partial y} + \dfrac{1}{\bar{\rho}}\dfrac{\partial^2 P}{\partial x\partial z} \\ -\dfrac{\partial\Gamma}{\partial x} + \dfrac{1}{\bar{\rho}}\dfrac{\partial^2 P}{\partial y\partial z} \\ -\dfrac{1}{\bar{\rho}}\dfrac{\partial^2 P}{\partial x^2} - \dfrac{1}{\bar{\rho}}\dfrac{\partial^2 P}{\partial y^2} \end{bmatrix}. \tag{A27}$$

The time stepping scheme for the horizontal passive scalar is different from that for the velocity or the entropy fluctuations. Since there are no vertical motions, the equation can be expressed in Fourier space in the following form:

$$\frac{\partial\hat{\phi}}{\partial t} + S_c(z_0)k^2\hat{\phi} = \hat{N}_\phi, \tag{A28}$$

with $N_\phi = -\nabla_h\cdot(\mathbf{u}\phi)$, and where z_0 is the height at which the passive scalar equation is solved. The dissipative term is treated exactly by an integrating factor; the nonlinear term is handled by a second order Adams-Bashforth scheme (with an Euler first step). The time discretization for the passive scalar therefore yields

$$\hat{\phi}^{n+1} = \exp\left(-S_c(z_0)k^2\Delta_t\right)\left(\hat{\phi}^n + \frac{3}{2}\Delta_t\hat{N}_\phi^n - \exp\left(-S_c(z_0)k^2\Delta_t\right)\frac{1}{2}\Delta_t\hat{N}_\phi^{n-1}\right). \tag{A29}$$

Note that the volume average of ϕ is constant over time, a fact that can be used to verify the accuracy of the code.

REFERENCES

Berkoff, N. A., Kersalé, E., & Tobias, S. M. 2010, GAFD, 104, 545. https://doi.org/10.1080/03091929.2010.521747

Boronski, P., & Tuckerman, L. S. 2007, JCoPh, 227, 1523. http://dx.doi.org/10.1016/j.jcp.2007.08.023

Braginsky, S. I., & Roberts, P. H. 1995, GAFD, 79, 1. https://doi.org/10.1080/03091929508228992

Bushby, P., Favier, B., Proctor, M., & Weiss, N. 2012, GAFD, 106, 508. https://doi.org/10.1080/03091929.2011.638067

Bushby, P. J., & Favier, B. 2014, A&A, 562, A72. https://doi.org/10.1051/0004-6361/201322993

Cattaneo, F. 1999, ApJ, 515, L39. http://stacks.iop.org/1538-4357/515/i=1/a=L39

Cattaneo, F., Emonet, T., & Weiss, N. 2003, ApJ, 588, 1183. http://stacks.iop.org/0004-637X/588/i=2/a=1183

Cattaneo, F., Lenz, D., & Weiss, N. 2001, ApJ, 563, L91. http://stacks.iop.org/1538-4357/563/i=1/a=L91

Clune, T., Elliott, J., Miesch, M., Toomre, J., & Glatzmaier, G. 1999, ParC, 25, 361 . http://www.sciencedirect.com/science/article/pii/S0167819199000095

Currie, L. K., & Tobias, S. M. 2016, PhFl, 28, 017101

Glatzmaier, G. A., & Gilman, P. A. 1981, ApJS, 45, 351

Gough, D. O. 1969, JAtS, 26, 448. https://doi.org/10.1175/1520-0469(1969)026<0448:TAAFTC>2.0.CO;2

Hathaway, D., Beck, J., Bogart, R., et al. 2000, SoPh, 193, 299. https://doi.org/10.1023/A:1005200809766

Hathaway, D. H., Teil, T., Norton, A. A., & Kitiashvili, I. 2015, ApJL, 811, 105. http://stacks.iop.org/0004-637X/811/i=2/a=105

Kupka, F., & Muthsam, H. J. 2017, Living Reviews in Computational Astrophysics, 3, 1. https://doi.org/10.1007/s41115-017-0001-9

Lantz, S. R., & Fan, Y. 1999, ApJS, 121, 247. http://stacks.iop.org/0067-0049/121/i=1/a=247

Lawrence, J. K., Cadavid, A. C., & Ruzmaikin, A. A. 1997, in Statistical Challenges in Modern Astronomy II, ed. G. J. Babu & E. D. Feigelson, 421

Mizerski, K. A., & Tobias, S. M. 2011, GAFD, 105, 566. https://doi.org/10.1080/03091929.2010.521748

November, L. J., Toomre, J., Gebbie, K. B., & Simon, G. W. 1981, ApJL, 245, L123

Rieutord, M., & Rincon, F. 2010, Living Reviews in Solar Physics, 7, 2. https://doi.org/10.12942/lrsp-2010-2

Rincon, F., Lignires, F., & Rieutord, M. 2005, A&A, 430, L57. https://doi.org/10.1051/0004-6361:200400130

Simon, G. W., & Weiss, N. O. 1989, ApJ, 345, 1060

Stix, M. 1989, The Sun: an Introduction (Springer-Verlag)

Verhoeven, J., Wiesehfer, T., & Stellmach, S. 2015, ApJ, 805, 62. http://stacks.iop.org/0004-637X/805/i=1/a=62